Composites Part B 313 (2026) 113399

Contents lists available at ScienceDirect

Composites Part B

journal homepage: www.elsevier.com/locate/compositesb

Waxberry-inspired aerogel metamaterial with gradient pore structure for superior electromagnetic wave absorption

Anping Wang [a], Zhichun Zhang [a,*], Yanju Liu [b,**], Jinsong Leng [a]

[a] Centre for Composite Materials and Structures, Harbin Institute of Technology (HIT), Harbin, 150080, People's Republic of China
[b] Department of Astronautic Science and Mechanics, Harbin Institute of Technology (HIT), Harbin, 150001, People's Republic of China

ARTICLE INFO

Keywords:
Aramid nanofiber
Carbon nanotube
Waxberry structure
Aerogel metamaterial
Electromagnetic wave absorption

ABSTRACT

Lightweight porous aerogels have demonstrated efficient electromagnetic wave absorption performance. Nevertheless, the inherent trade-off between favorable impedance matching at the atmosphere-aerogel interface and strong electromagnetic loss within the aerogel matrix has limited the further improvement of the aerogel's electromagnetic wave absorption performance. In this study, a waxberry-inspired gradient-porous aerogel metamaterial (WGAM) was successfully fabricated via an innovative dot-matrix cooling source ice templating technique. The influences of diverse pore structures and repeating unit sizes on the performance of aerogels were systematically investigated and analyzed. The results reveal that the gradient pore structure in WGAM effectively balances the conflict between interface impedance matching and intrinsic electromagnetic loss, enabling WGAM to achieve an ultrabroad effective absorption bandwidth of 12.3 GHz within the range of 2–18 GHz. Meanwhile, owing to the 3D radial distribution of internal pores, WGAM retains robust electromagnetic wave absorption capacity even when the incident angle of electromagnetic waves is increased from 5° to 30°. Furthermore, WGAM exhibits favorable mechanical, thermal-insulating, and flame-retardant properties, rendering it a promising candidate for electromagnetic protection applications under complex and harsh environmental conditions.

1. Introduction

While radio communication technologies have brought tremendous convenience to human life, they have concomitantly caused severe electromagnetic radiation pollution, which poses non-negligible threats to information transmission security, military operational concealment, and human physiological health [1–4]. To mitigate these predicaments, electromagnetic wave absorption (EMWA) materials have been identified to possess the capability to efficiently dissipate and absorb electromagnetic waves (EMWs), thereby demonstrating superior advantages in alleviating electromagnetic radiation pollution [5]. In particular, aerogels simultaneously possess ultra-low density and excellent EMWA performance, which facilitates the lightweight of EMWA devices and thus holds significant research value [6,7].

Currently, the optimization of EMWA performance in aerogels can be achieved through rational structure design and construction [8–10]. For instance, drawing inspiration from the dual-channel transport mechanism of vascular bundles within plant phloem-xylem networks, Su et al. have engineered an Absorption-Transport Multifunctional Structure (ATMS), which exhibits frequency-selective characteristics, characterized by high transmittance in the low-frequency band (2.0–2.56 GHz) and remarkable absorption efficiency in the high-frequency band (9.16–11.93 GHz) [11]. Moreover, the pore orientation of aerogels exerts a pivotal influence on their EMWA performance [12,13]. For example, Xu et al. [14] fabricated CNT/C@Si_3N_4 aerogels with an oriented architecture via the unidirectional freezing ice templating method. The results demonstrated that when EMWs are incident along the direction perpendicular to the oriented pores, the minimum reflection loss (RL_{min}) of the aerogels reaches −28 dB at 11.0 GHz, and the effective absorption bandwidth (EAB) can cover the entire X-band (8.2–12.4 GHz). In contrast, when EMWs are incident along the direction parallel to the oriented pores, the RL_{min} of the aerogels decreases to −12 dB at 12.4 GHz, accompanied by a narrowed EAB of 2.3 GHz (10.1–12.4 GHz). The underlying mechanism accounting for this discrepancy is that EMWs incident along the direction perpendicular to the oriented pores encounter more pore cavities and heterogeneous pore

* Corresponding author.
** Corresponding author.
E-mail addresses: zczhang@hit.edu.cn (Z. Zhang), yj_liu@hit.edu.cn (Y. Liu).

https://doi.org/10.1016/j.compositesb.2026.113399
Received 24 November 2025; Received in revised form 30 December 2025; Accepted 8 January 2026
Available online 13 January 2026

wall interfaces, inducing multiple reflections and scattering losses that extend the EMW transmission path. Consequently, regulating the pore orientation within aerogels constitutes an effective approach to optimizing their EMWA performance [15,16].

A rationally engineered gradient structure can alleviate the inherent contradiction between excellent interface impedance matching and strong internal dielectric loss [17–21]. For instance, Yu et al. [22] constructed a concentration gradient of EMW absorbent along the thickness direction of the aerogel: the low-concentration EMW absorbent in the upper layer facilitates the atmosphere-aerogel interfacial impedance matching, reduces the reflection of incident EMWs at the interface, and allows more EMWs to penetrate the aerogel interior; conversely, the high-concentration EMW absorbent in the lower layer enables efficient dissipation and absorption of EMWs. Furthermore, Sun et al. [23] designed aerogel metamaterials with a frustum pyramid shape, which realize an impedance gradient structure along the thickness direction and induce multiple resonances between structural units, significantly broadening the EAB. It follows that regulating the concentration gradient of absorbents or engineering geometric gradients of aerogels along the thickness direction can notably balance the trade-off between impedance matching and dielectric loss. However, achieving a concentration gradient of EMW absorbents typically requires the preparation of EMW absorbents with multiple concentrations, which renders the fabrication process time-consuming and labor-intensive [24]. Additionally, conventional EMW absorbers feature irregular geometries such as wedges, frustums, or step-like structures, posing considerable challenges for the assembly and integration of final EMW absorber devices. Therefore, there is an urgent imperative to design an aerogel structure that simultaneously meets the following two criteria: (I) A gradient variation in characteristic impedance and EMW loss capability can be achieved along the thickness direction of the aerogel using a single absorbent formulation. (II) The EMW absorber device exhibits a regular shape.

In this work, inspired by the radial flesh and dense core structure of natural waxberries, we developed a dot cooling source ice templating method to regulate ice crystal growth direction, thereby constructing a waxberry-like radial gradient pore and central core structure inside the aerogel. Specifically, the radial gradient pores optimize the atmosphere-aerogel interface impedance matching, while the dense core enhances the dielectric loss capability. Furthermore, through the periodic matrix arrangement of dot cooling sources, we successfully fabricated a waxberry-inspired gradient-porous aerogel metamaterial (WGAM). WGAM can achieve a gradient variation of impedance along the thickness direction with only a single absorbent filler formulation, effectively resolving the contradiction between impedance matching and dielectric loss. Combined with the coupling effect between the periodic structural units of the metamaterial, WGAM exhibits an ultrabroad EAB of 12.3 GHz. More importantly, WGAM demonstrates insensitivity to the incident angle of EMWs ranging from 5° to 30°. In addition, WGAM features a regular macroscopic shape, which significantly improves the assembly and integration efficiency of EMWA devices. Moreover, benefiting from the intrinsic properties of aramid nanofiber (ANF) as well as the bio-inspired waxberry-like porous structure, WGAM demonstrates excellent thermal-insulating, flame-retardant, and mechanical properties. Owing to its facile molding process, regular device morphology, and outstanding comprehensive performance, WGAM holds substantial potential for deployment in complex environments such as aerospace, anechoic chambers, and marine vessels.

2. Experimental section

2.1. Materials

Chopped PPTA thread (Kevlar 49) was purchased from DuPont, China. Carboxylated multi-walled carbon nanotube (c-MWCNT, diameter: 10–30 nm, length: 10–30 μm, purity: 98 %) was obtained from Chengdu Organic Chemicals Co., Ltd., Chinese Academy of Sciences. Dimethyl sulfoxide (DMSO), methanol (MeOH), potassium tert-butoxide (t-BuOK), and acetic acid (HAc) were supplied by Aladdin Scientific Chemicals, Shanghai.

2.2. Preparation of c-MWCNT/ANF composite dispersions

To tailor the filler ratio of c-MWCNT/ANF composite dispersions, the mass ratio of c-MWCNT to ANF was adjusted, and the resulting samples were denoted as CxAy. Specifically, C corresponds to c-MWCNT, A to ANF, where x and y denote the mass ratios of c-MWCNT and ANF, respectively. Accordingly, four sets of composite dispersions (C2A1, C3A1, C4A1, and C5A1) were fabricated, corresponding to filler ratios of 2:1, 3:1, 4:1, and 5:1. Notably, the total mass fraction of c-MWCNT and ANF was fixed at 5 wt% across all composite dispersions, thereby ensuring that only the filler ratio was varied as the sole experimental variable.

Taking the preparation process of the C4A1 dispersion as an example. First, short-cut Kevlar 49 fibers (2 g), DMSO (94 g), MeOH (2 g), and t-BuOK (2 g) were sequentially added to a 500 mL conical flask, which was then tightly sealed. The mixture was magnetically stirred at room temperature for 48 h to obtain a wine-red translucent 2 wt% ANF solution [25]. Subsequently, c-MWCNT powder (8 g) and DMSO (92 g) were sequentially added to a 500 mL beaker. The mixture was treated with 300 W probe sonication for 10 min followed by high-speed stirring at 8000 rpm for 10 min, affording an 8 wt% c-MWCNT slurry. Finally, equal masses of the as-prepared ANF solution and c-MWCNT slurry were mixed and magnetically stirred for 4 h to form a homogeneous c-MWCNT/ANF composite dispersion.

2.3. Preparation of waxberry gradient-porous aerogel metamaterials (WGAM)

Herein, the fabrication process of a waxberry gradient-porous C4A1 aerogel metamaterial with a repeating unit of 10 mm (WC4A1-10 mm) is presented as an example to illustrate the preparation methodology. First, a dot-matrix cooling source mold (Fig. 1b) was designed to control the periodic 3D radial growth of ice crystals. The mold base and frame were constructed from polytetrafluoroethylene (PTFE), with internal dimensions of 50 × 50 × 20 mm and a wall thickness of 5 mm. Through-holes with a diameter of 3 mm were drilled at 10 mm intervals on the mold base, into which high-thermal-conductivity copper rods (55 mm in length, 3 mm in diameter) were inserted. Subsequently, the prepared C4A1 composite dispersion was poured into the mold, with the liquid level height in the mold reaching 10 mm. The mold was then slowly immersed in a 1 wt% acetic acid solution for a 24-h gelation reaction. After complete gelation, the mold was soaked in deionized water to remove residual acetic acid. Finally, the lower ends of the copper rods were immersed in liquid nitrogen, and heat was transferred through the dot-matrix cooling source to induce the 3D radial growth of ice crystals. After the sample was completely frozen, it was transferred to a freeze dryer and subjected to sublimation drying at 0.5 Pa for 48 h to remove the ice crystals while retaining the hierarchical porous structure, thus obtaining WC4A1-10 mm. To investigate the influence of c-MWCNT contents on the EMWA performance, WC2A1-10 mm, WC3A1-10 mm, and WC5A1-10 mm were fabricated by the same preparation process. In addition, we investigated the effect of the unit size on the EMWA performance of WGAM by keeping the ratio of the total area of cooling sources to the base area constant. As shown in Fig. S8c, the diameter of the copper rods was increased to 6 mm with a spacing of 20 mm, and a waxberry pore-structured C4A1 aerogel metamaterial with a repeating unit of 20 mm (WC4A1-20 mm) was prepared. Similarly, the diameter of the copper rods was adjusted to 9 mm with a spacing of 30 mm (Fig. S8d), thus preparing a waxberry pore-structured C4A1 aerogel metamaterial with a repeating unit of 30 mm (WC4A1-30 mm).

The preparation processes of balsa-wood pore-structured aerogels

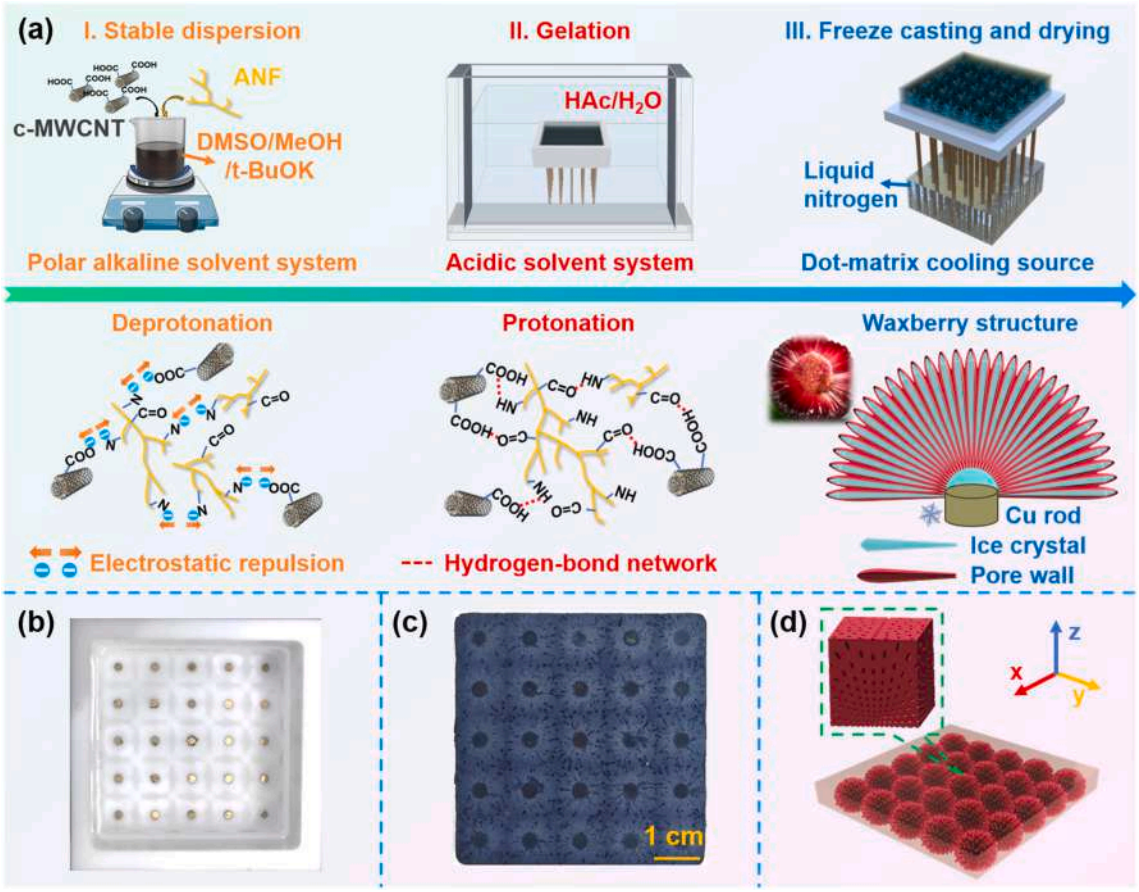

Fig. 1. Schematic diagram and photographs. (a) The preparation process and mechanism of WGAM. (b) dot-matrix cooling source mold for preparing WGAM. (c) bottom photograph and (d) schematic diagram of WGAM matrix structure.

(BPA) and randomly porous aerogels (RPA) are provided in the Supplementary Material. Specifically, the BPA with a filler ratio of C4A1 is denoted as BC4A1. For the RPA samples, those with filler ratios of C2A1, C3A1, C4A1, and C5A1 are abbreviated as RC2A1, RC3A1, RC4A1, and RC5A1, respectively.

2.4. Characterization

The morphological characteristics of the aerogels were examined using a scanning electron microscope (SEM, VEGA3, TESCAN, Czech Republic) operated at an accelerating voltage of 20 kV and 3D Computed Tomography (3D-CT, Xradia 520 Versa, Zeiss, USA). The diameter of c-MWCNT was characterized using a transmission electron microscope (TEM, JEM-F200, JEOL, Japan). The diameter of ANF was determined using an atomic force microscope (AFM, Smart SPM, AIST-NT, USA). Fourier transform infrared spectroscopy (FTIR, Spectrum Two, PerkinElmer, UK) was employed to characterize the functional groups and hydrogen bonding interactions. An X-ray diffractometer (XRD, Empyrean, PANalytical, the Netherlands) was utilized to analyze the crystal lattice structures, with a scanning rate of 5° min^{-1} and a 2θ range of 5°–90°. The chemical structures were analyzed via a Raman imaging microscope spectrometer (inVia-Reflex, RENISHAW, UK) equipped with a 532 nm laser source. The elemental compositions of the specimens were determined by X-ray photoelectron spectroscopy (XPS, ESCALAB 250Xi, Thermo-Fisher, USA) with a monochromatic Al Kα radiation source. Thermal conductivities were measured using a hot disk thermal constant analyzer (Hot Disk, TPS 2500S, Sweden). Compression tests were conducted with a universal testing machine (Instron, USA) at a strain of 30 % and a compression rate of 1 mm min^{-1}. The thermal stability of the samples was evaluated using a thermogravimetric analyzer (TGA 1, Mettler Toledo, Switzerland) under a nitrogen atmosphere, with a heating rate of 10 °C·min^{-1} over a temperature range from 40 °C to 1000 °C. The relative complex permittivity and permeability within the frequency range of 2–18 GHz were measured using a vector network analyzer (E5071C, Agilent, USA) via the coaxial line method. The molten paraffin was infiltrated into the RPA (RC2A1, RC3A1, RC4A1, and RC5A1) under vacuum assistance at 100 °C, the mass ratio of aerogel to paraffin was controlled at approximately 7 wt% to 93 wt%. After cooling and solidification, the RPA/paraffin composites were cut into coaxial rings with an outer diameter of 7 mm and an inner diameter of 3.04 mm. The reflection loss values in the frequency range of 2–18 GHz were measured in situ using the arch method and a vector network analyzer (Ceyear Technologies 3672C–S), as illustrated in Fig. S13. The aerogels were periodically positioned on a 5 mm-thick aluminum plate. To evaluate the angle-dependent properties of the samples, the incident angles of EMWs were adjusted to 5°, 15°, 30°, 45°, and 60°. The simulation of electromagnetic power loss was performed using CST Studio Suite. The simulation of heat transfer was conducted via COMSOL Multiphysics. (Detailed modeling and simulation parameters are provided in the Supplementary Material).

3. Results and discussion

3.1. Fabrication strategy and mechanism

The selection of materials plays a crucial role in the preparation process and comprehensive performance of aerogels. c-MWCNT exhibits excellent EMWA properties and can meet the requirements of aircraft for lightweight. However, c-MWCNT faces challenges such as easy agglomeration and difficult molding during the aerogel processing. The

introduction of ANF can address the aforementioned issues. ANF inherits the advantages of Kevlar fibers, such as high-temperature resistance, flame retardancy, and high mechanical strength [26]. Additionally, ANF exhibits a branched structure (Fig. S9c) and has an approximate diameter of 7.7 nm (Fig. S9d), both of which can significantly enhance its interfacial interaction with c-MWCNT [27,28]. Most importantly, the deprotonation and protonation reactions of ANF in different solvent systems enable the regulation of intermolecular interactions [29]. In the strongly polar alkaline solvent system of DMSO/MeOH/t-BuOK, ANF and c-MWCNT undergo deprotonation, causing their molecular chains to carry negative charges and generate electrostatic repulsion forces (Fig. 1a). Under the action of electrostatic repulsion forces, ANF and c-MWCNT achieve uniform dispersion and avoid agglomeration. Subsequently, solvent replacement is carried out in an aqueous HAc solution. HAc provides abundant hydrogen protons, which facilitate c-MWCNT and ANF to form a 3D hydrogen-bond network, promoting the gelation transformation of the composite dispersion (Fig. S7).

The impedance matching and EMW loss capabilities of aerogels are closely related to their internal microscopic pore structures. To enable aerogels to simultaneously exhibit excellent impedance matching and wave absorption loss, constructing a gradient structure within the aerogel is an effective strategy. Inspired by the radial and gradient pore structure of natural waxberries, we designed dot cooling sources to control the 3D radial growth of ice crystals inside the hydrogel during freezing. Furthermore, by arranging the dot cooling sources in a periodic matrix at the bottom of the mold, periodic waxberry pore-structured units are constructed inside the aerogel, thereby forming a waxberry pore-structured aerogel metamaterial (Fig. 1b–d).

3.2. Microstructural and morphological analysis

As depicted in Fig. 2a, upon freezing within the dot-matrix cooling source mold, water gives rise to regularly arranged repeating units, with ice crystals inside each unit exhibiting a radial distribution pattern around the center. By tracking the growth process of ice crystals induced by two adjacent dot cooling sources, it is observed that nucleation initiates at the copper rods, followed by radial outward growth. Eventually, the ice crystals collide and fuse at the interface of two repeating units

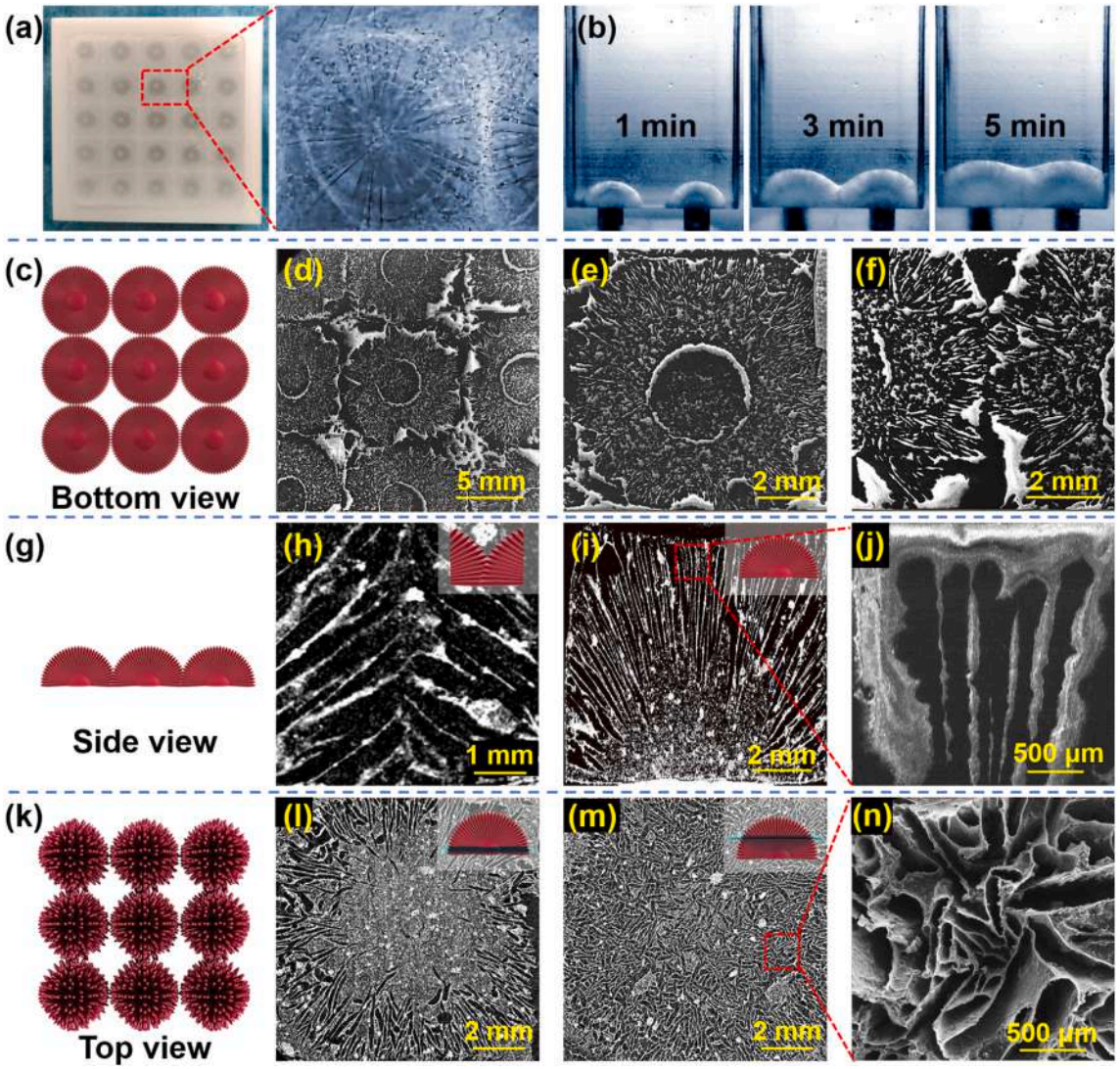

Fig. 2. Microstructural and morphological analysis. (a) Morphology and (b) growth process of ice crystals within the dot-matrix cooling source mold. Bottom view: (c) schematic illustration of the bottom structure; SEM images of (d) waxberry-like matrix structure, (e) single waxberry structural unit, and (f) junction of two repeating waxberry structural units. Side view: (g) schematic illustration of the side structure; CT slices of (h) pore structure at the junction of two units and (i) waxberry-like radial pore structure and core structure; (j) SEM image of radial structure with gradient change in pore size. Top view: (k) schematic illustration of the top structure; CT slices of (l) lower half section of the xy-plane along the z-axis direction and (m) upper half section of the xy-plane along the z-axis direction; (n) SEM image of horn-shaped opening structure.

(Fig. 2b and Video S1).

Supplementary data related to this article can be found online at https://doi.org/10.1016/j.compositesb.2026.113399

To visually analyze the pore structure of WGAM, Scanning Electron Microscopy (SEM) and 3D Computed Tomography (3D-CT) were employed to characterize and analyze the microtopography of the aerogels. Firstly, the microstructure of WGAM was observed from the bottom. As shown in Fig. 2c and d, WGAM fabricated by the dot-matrix cooling source ice templating method exhibits a periodic waxberry-like metamaterial array. Fig. 2e shows the morphological characteristics of a structural unit at the bottom of WGAM. It can be observed that a waxberry-like core structure is formed at the position in direct contact with the copper rod, and with this core as the center, the pore structure of WGAM distributes radially toward the surrounding area. Fig. 2f presents the morphological features at the junction of two structural units, from which it can be observed that the two waxberry structures are tightly connected.

Subsequently, CT slices were performed at the central part of the WGAM structural unit along the xz plane (refer to the coordinates in Fig. 1d) to observe the pore distribution and orientation of the WGAM's side cross-section (Fig. 2g). Fig. 2h presents a CT slice of the WGAM's side cross-section at the junction of two structural units, where the pores exhibit a symmetrical distribution. As shown in Fig. 2i and Fig. S11, the pores of WGAM distribute radially from the bottom center to the surrounding area in a single structural unit, confirming that the dot cooling source can successfully control the growth direction of ice crystals. The locally enlarged view in Fig. 2j reveals that the pore size of WGAM gradually increases from bottom to top along the z-axis direction. The horn-shaped gradient pore structure is beneficial for improving the impedance-matching ability of WGAM. Finally, CT slices were performed along the xy plane in the lower half (Fig. 2l) and upper half (Fig. 2m) of WGAM to observe the variation of pores along its thickness direction, respectively. In the lower half (Fig. 2l), the central pores of WGAM are relatively dense, corresponding to the core in the waxberry-like structure; the edge pores distribute radially from the central core, resembling the flesh in the waxberry-like structure. In the upper half (Fig. 2m), the pores of WGAM are uniformly distributed with openings facing upward, and the horn-shaped pore structure can be observed in the locally enlarged view (Fig. 2n).

3.3. Composition analysis

XRD is used to characterize and analyze the crystal structure of materials. As shown in Fig. 3a, c-MWCNT exhibits a sharp diffraction peak at approximately 26.0°, which corresponds to the typical (002) crystal plane, reflecting the interlayer stacking of c-MWCNT. In addition, c-MWCNT has a weaker diffraction peak at around 42.7°, corresponding to the planar arrangement of carbon six-membered rings on the (100) crystal plane. ANF shows two diffraction peaks with similar intensities at approximately 20.0° and 23.1°, corresponding to the (110) and (200) crystal planes, respectively, which reflect the periodic arrangement of ANF molecular chains along the fiber axis [30]. In the c-MWCNT/ANF composites, due to the excessively high intensity of the c-MWCNT diffraction peaks, which mask the diffraction peaks of ANF, only the obvious (002) and (100) crystal planes are observed in the pattern.

Raman spectroscopy was employed to characterize and analyze the molecular structure of materials (Fig. 3b). The Raman spectrum of c-MWCNT exhibits three characteristic peaks: the D band (1333.5 cm^{-1}), G band (1564.9 cm^{-1}), and 2D band (2679.6 cm^{-1}). Among them, the D band is attributed to the resonance caused by defects in the disordered carbon within the c-MWCNT lattice, while the G band corresponds to the in-plane tangential vibration of ordered sp^2-hybridized carbon atoms. In the Raman spectrum of ANF, the characteristic peak at 1603.5 cm^{-1} represents the in-plane stretching vibration of C═C bonds in the benzene ring skeleton, and the peak at 1645.9 cm^{-1} is assigned to the C═O stretching vibration. The three characteristic peaks in the range of 1150~1370 cm^{-1} result from the coupling of C–N stretching vibrations and N–H bending vibrations. In the c-MWCNT/ANF spectrum, the excessively high intensity of the characteristic peaks of c-MWCNT partially masks those of ANF. The defect degree of the carbon lattice in carbon nanotubes can be evaluated by the intensity ratio of the D band to the G band (I_D/I_G). For c-MWCNT, the I_D/I_G ratio is 0.86, while that of c-MWCNT/ANF is 0.8. The decrease in the I_D/I_G ratio may be attributed to the interaction forces between c-MWCNT and ANF, which affect the vibration of disordered carbon in c-MWCNT.

Fourier transform infrared (FTIR) spectroscopy was utilized to detect the organic functional groups in the materials and to provide evidence for the existence of interaction forces between c-MWCNT and ANF. As shown in Fig. 3c, for c-MWCNT, a stretching vibration peak of O–H

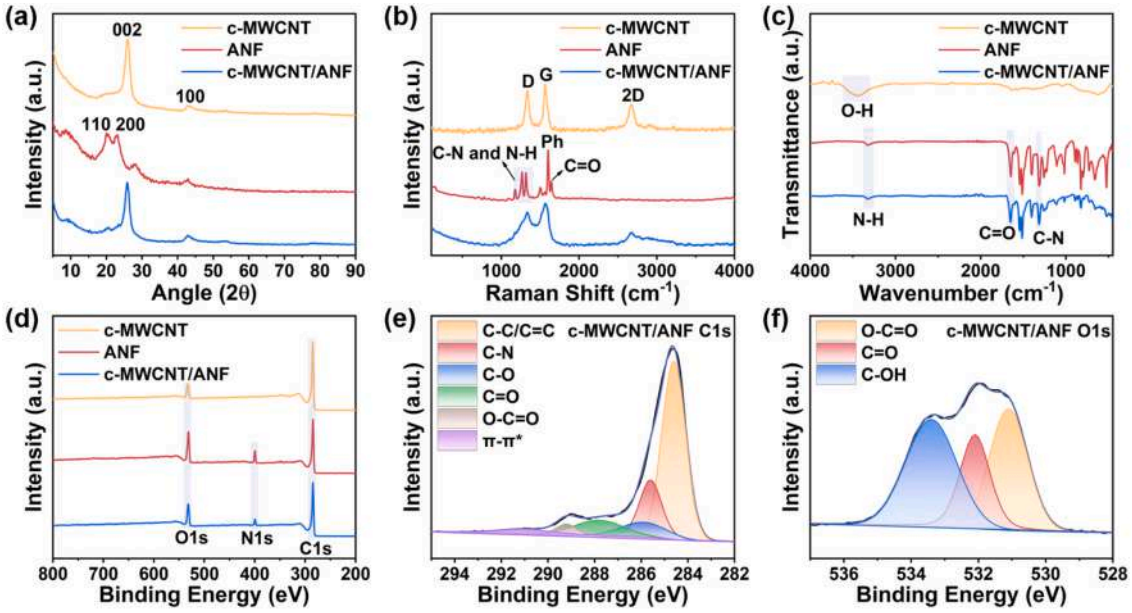

Fig. 3. Material composition analysis. (a) XRD spectra; (b) Raman spectra; (c) FTIR spectra; (d) XPS spectra; (e) XPS C1s spectra of c-MWCNT/ANF; (f) XPS O1s spectra of c-MWCNT/ANF.

groups appears at 3340 cm^{-1}, which confirms that the surface of c-MWCNT is rich in oxygen-containing functional groups. For ANF, the stretching vibration peaks at 3325 cm^{-1}, 1646 cm^{-1}, and 1314 cm^{-1} correspond to N–H, C═O, and C–N groups, respectively [31]. In the case of c-MWCNT/ANF, the stretching vibration peaks at 3325 cm^{-1}, 1650 cm^{-1}, and 1316 cm^{-1} are assigned to N–H, C═O, and C–N groups, respectively. By comparing the infrared absorption peaks of ANF and c-MWCNT/ANF, it is found that the absorption peaks of C═O and C–N have undergone a shift, which may be attributed to the formation of hydrogen bonds between c-MWCNT and ANF.

X-ray photoelectron spectroscopy (XPS) can be used to detect and analyze the elemental composition and chemical functional groups on the surface of materials. As shown in Fig. 3d and Table S1, c-MWCNT exhibits two peaks, namely C 1s (~285 eV) and O 1s (~533 eV), among which O 1s accounts for 8.41 at.%, indicating that the surface of c-MWCNT contains abundant oxygen-containing functional groups. These functional groups can enhance the chemical and physical activity of c-MWCNT. The c-MWCNT/ANF shows three peaks: C 1s (~285 eV), O 1s (~532 eV), and N 1s (~400 eV). The presence of N 1s (4.23 at.%) is mainly due to the introduction of ANF. The C 1s spectrum of c-MWCNT/ANF was deconvoluted into six peaks (Fig. 3e), which correspond to C–C/C═C (284.6 eV), C–N (285.6 eV), C–O (285.9 eV), C═O (287.8 eV), O–C═O (289.2 eV), and π–π* (291.0 eV), respectively. Similarly, the O 1s spectrum of c-MWCNT/ANF was deconvoluted into three peaks (Fig. 3f), which are assigned to O–C═O (531.1 eV), C═O (532.1 eV), and C–O (533.4 eV), respectively [32]. These polar functional groups can generate dipole polarization under high-frequency EMWs to effectively dissipate them, thereby improving the EMWA performance of the aerogel.

3.4. Electromagnetic wave absorption performance

The complex permittivity (real part of permittivity ε' and imaginary part of permittivity ε'') and complex permeability (real part of permeability μ' and imaginary part of permeability μ'') are used to analyze the electromagnetic properties of materials. Since the c-MWCNT/ANF aerogel is a typical dielectric loss EMWA material without magnetic loss, μ' and μ'' are close to 1 and 0, respectively. Therefore, only ε' and ε'' are considered in this paper. In the frequency range of 2–18 GHz, the electromagnetic parameters of RPA with different c-MWCNT and ANF filler ratios were tested by the coaxial method. As shown in Fig. 4a and b, ε' and ε'' exhibits a decreasing trend with increasing frequency, which is consistent with the dielectric relaxation phenomenon described by Debye theory [33]. Additionally, the permittivity-frequency curves exhibit noticeable fluctuations, which can be attributed to the coexistence of macropores and micropores within the RPA. These pores display distinct polarization relaxation behaviors as frequency increases, thereby directly inducing the observed fluctuations. Furthermore, multiple interfaces (c-MWCNT-ANF, c-MWCNT-paraffin, and ANF-paraffin) exist in the RPA, each of which exhibits distinct frequency-dependent charge accumulation characteristics, thus amplifying the fluctuations in the permittivity-frequency response profiles [34,35]. With the increase in c-MWCNT content, the values of ε', ε'', dielectric loss tangent ($\tan\delta\varepsilon = \varepsilon''/\varepsilon'$), and attenuation constant (α) gradually increase (Fig. 4a–d), indicating that the conductive network formed by c-MWCNT is gradually improved, and the dielectric loss capacity of the material for EMWs is gradually enhanced. α is generally used to evaluate the capability of EMWA materials to convert incident EMW energy into other forms of energy. As the frequency of EMWs increases, the α value

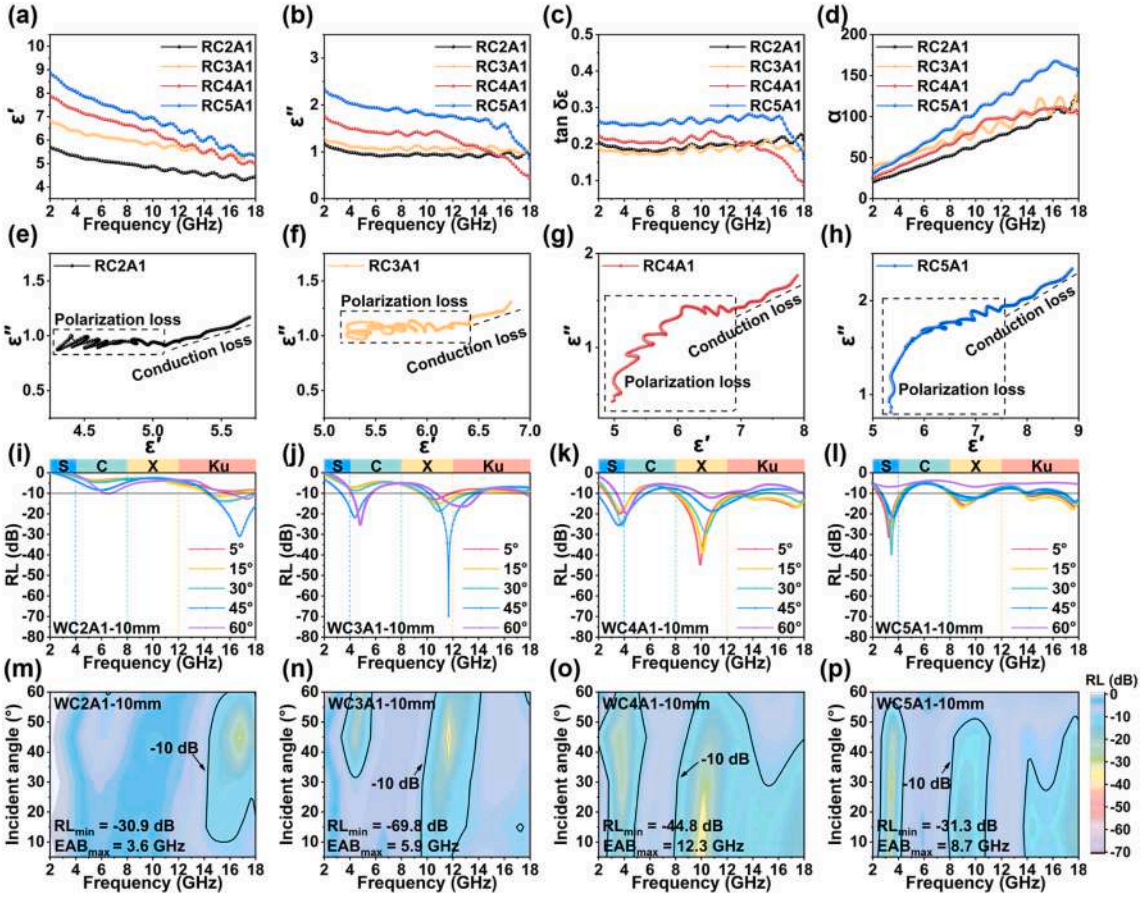

Fig. 4. Effect of filler ratio on electromagnetic parameters and EMWA properties. RPA with different filler proportions: (a) Real part of permittivity, (b) Imaginary part of permittivity, (c) Dielectric loss tangent, (d) Attenuation constant, (e–h) Cole-Cole curves. WGAM with different filler proportions: (i–l) 2D RL_{min}-f-IA curves and (m–p) 2D RL_{min}-f-IA mapping diagrams.

of the aerogel gradually increases. The Cole-Cole curve can be used to analyze the loss mechanisms existing in EMWA materials. As shown in Fig. 4e–h, for the Cole-Cole curve, the multiple semicircles represent polarization losses (interface polarization and dipole polarization of nanomaterials) under high-frequency electromagnetic fields, while the long straight linear tail corresponds to conductive losses generated by the c-MWCNT network. This confirms that the c-MWCNT/ANF aerogels exhibit multiple loss mechanisms for EMWs.

In a microwave anechoic chamber, the reflection loss of WGAM with different carbon nanotube contents was tested using the arch method (Fig. S13). Additionally, the angle of the horn antenna was adjusted to investigate the effect of EMW incident angles (IA = 5°, 15°, 30°, 45°, and 60°) on the EMWA performance of WGAM. For WC2A1-10 mm (Fig. 4i and m), when the IA is 5°, the RL_{min} is greater than −10 dB in the 2–18 GHz band, and the EAB is 0 GHz. When the IA increases within the range of 5°–45°, the EMWA performance of WC2A1-10 mm improves. For instance, when the IA increases to 45°, the RL_{min} of WC2A1-10 mm reaches −30.9 dB at 16.8 GHz, with an EAB of 3.6 GHz. However, when the IA further increases to 60°, the RL_{min} decreases to −12.7 dB at 17.4 GHz, and the EAB reduces to 2.4 GHz. For WC3A1-10 mm (Fig. 4j and n), when the IA is 45°, the RL_{min} reaches −69.8 dB at 11.7 GHz, which is the strongest reflection loss among all samples. For WC4A1-10 mm (Fig. 4k and o), when the IA is 5°, the RL_{min} is −44.8 dB at 9.9 GHz, and the EAB reaches 12.3 GHz, which is the widest effective absorption bandwidth among all samples. Moreover, within the IA range of 5°–30°, the EAB of WC4A1-10 mm is greater than 11.3 GHz, indicating that the electromagnetic parameters when the c-MWCNT content is C4A1 can effectively balance impedance matching and loss absorption. For WC5A1-10 mm (Fig. 4l and p), when the IA is 5°, the RL_{min} is −31.3 dB at 3.3 GHz, and the EAB is 8.7 GHz, exhibiting excellent EMWA performance in the low-frequency band. It can be concluded from the test results that regulating the EMWA performance of WGAM requires comprehensive consideration of two aspects: the ratio of absorbents (electromagnetic parameters) and the incident angle of EMWs (matching thickness).

In addition, we further investigated the effects of the orientation structure of internal pores and the size of repeating units of the aerogels on their EMWA performance. For the convenience of analysis, the c-MWCNT ratio of C4A1 was selected to explore the influence. Herein, we designed a uniform cooling source mold (Fig. S8a), a single-sided cooling source mold (Fig. S8b), and dot-matrix cooling source molds with different sizes (Fig. 1b, Fig. S8c and S8d) to control the growth direction of ice crystals during solution freezing, thus preparing RC4A1, BC4A1, WC4A1-10 mm, WC4A1-20 mm, and WC4A1-30 mm.

As shown in Fig. 5a and Fig. S14, the RL and EAB of aerogels with

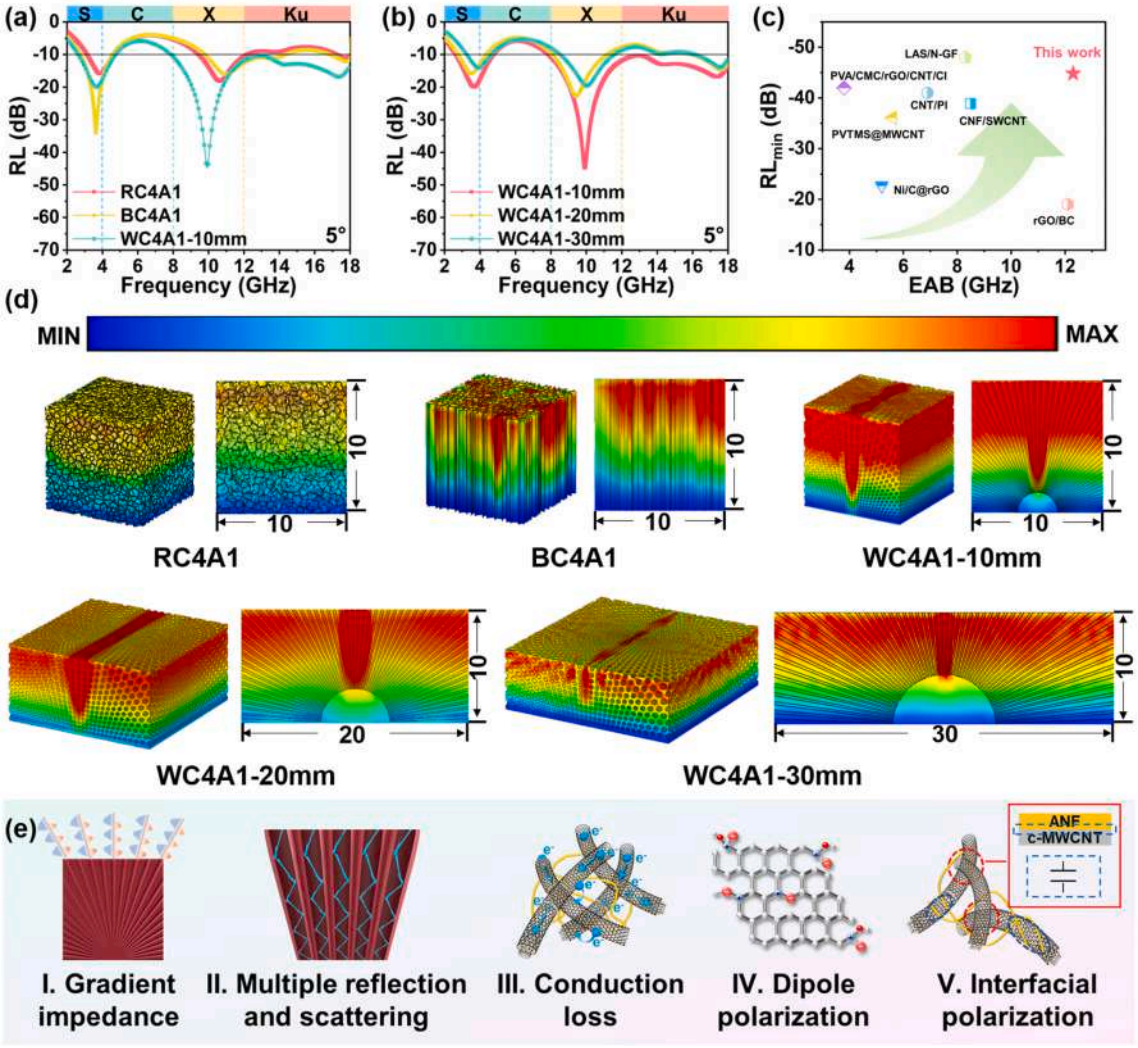

Fig. 5. Effect of pore structure and repeat unit size on EMWA properties. (a) 2D RL_{min}-f-IA curves of aerogels with different pore structures. (b) 2D RL_{min}-f-IA curves of WGAM with different repeating unit sizes. (c) Comparison of RL_{min} and EAB performance with previously reported non-graded structure aerogels. (d) Power loss density distribution diagrams of aerogels with different pore structures and repeating unit sizes (the unit of length for the model is millimeters). (e) Schematic diagram of the WGAM wave-absorbing mechanism.

different oriented structures are compared. When the IA is 5°, the RL_{min} of RC4A1 is −18.1 dB with an EAB of 5.0 GHz; the RL_{min} of BC4A1 is −34.0 dB with an EAB of 7.6 GHz; and the RL_{min} of WC4A1-10 mm is −44.8 dB with an EAB of 12.3 GHz. It can be observed that the EMWA performance of the WGAM is superior to that of the RPA and the BPA. This is attributed to the fact that WGAM possesses horn-shaped pores, which endow the aerogel with a gradient variation of impedance along the z-axis. Along the z-axis upward, WGAM exhibits a gradual increase in pore diameter and a progressive rise in porosity, making the impedance of the upper surface close to atmospheric impedance. When EMWs are incident on WGAM, the atmosphere-aerogel interface satisfies the characteristic of impedance matching. This reduces reflections at the atmosphere-aerogel interface, thereby significantly enhancing the EMWA performance. In addition, compared with RPA and BPA, WGAM exhibits insensitivity to the incident angle of EMWs. As illustrated in Fig. S15a and S15b, when EMWs are incident upon RPA and BPA at an oblique angle, their propagation is obstructed by the pore walls. However, WGAM features a radial distribution of pores (Fig. S15c). When EMWs strike WGAM at oblique angles ranging from 5° to 30°, some pores are aligned with the incident direction of EMWs, enabling the EMWs to penetrate into the interior of WGAM. Further, EMWA is achieved through mechanisms such as multiple reflection loss, conductive loss, and polarization loss. Therefore, WGAM demonstrates insensitivity to the incident angle of EMWs.

Fig. 5b and Fig. S16 compare the EMWA properties of WC4A1 with different repeating unit sizes. At an IA of 5°, WC4A1-20 mm exhibits an RL_{min} of −22.7 dB with an EAB of 6.7 GHz, while WC4A1-30 mm shows an RL_{min} of −19.6 dB and an EAB of 6.3 GHz. It can be observed that the EMWA performance of WGAM tends to decrease as the size of the repeating units increases, and the underlying reason will be explained with subsequent simulation results. Fig. 5c and Table S5 present a performance comparison of the RL_{min} and EAB between WGAM and previously reported non-graded structural aerogels [36–42]. Thanks to the gradient variation of the waxberry-like pore structure, WGAM exhibits significantly superior EMWA performance compared to traditional non-graded structural aerogels.

Finite element simulation offers a robust approach to analyzing the loss distribution of EMWs in aerogels with distinct pore structures. In this work, aerogels with varied structural configurations were first modeled using 3D modeling software packages, followed by electromagnetic field simulations conducted via the finite element software CST Studio Suite 2025 (Detailed modeling and simulation parameters are provided in the Supplementary Material). Fig. 5d illustrates the power loss density of aerogels with different structures under identical incident EMW conditions. By comparing the aerogels with three distinct pore architectures (RC4A1, BC4A1, and WC4A1-10 mm), it is evident that WC4A1-10 mm exhibits the highest power loss density. This superior performance stems from the waxberry-like gradient pore structure, which endows the WC4A1-10 mm with an impedance gradient along the z-axis. Such an impedance gradient enables incident EMWs to penetrate deeply into the aerogel interior, while the radial pore structure extends the propagation path of EMWs within the aerogel through multiple reflections and scatterings. Furthermore, a comparison of the power loss density distribution profiles among WC4A1-10 mm, WC4A1-20 mm, and WC4A1-30 mm reveals that WC4A1-10 mm achieves the maximum power loss density. This phenomenon may be ascribed to the excessively large inclination angle of the pores at the top edge of WGAM as the repeating unit size increases (Fig. S11), which impedes the penetration of EMWs into the aerogel interior and thereby results in a deterioration of loss capacity. These simulation results are consistent with the experimentally determined EMWA performance of the aerogels.

Fig. 5e illustrates the potential EMWA mechanisms of WGAM. (I) Gradient impedance: WGAM features radial horn-shaped pores, which induce a gradient impedance along the z-axis. The impedance near the upper surface of WGAM is close to the atmospheric impedance, satisfying the characteristic of impedance matching and thus reducing the reflection of incident EMWs at the interface [43,44]. Conversely, along the thickness direction of the WGAM from top to bottom, the pore size decreases gradually, and the corresponding impedance drops correspondingly, thereby achieving efficient dissipation of incident EMWs. (II) Multiple reflection and scattering: The WGAM matrix contains an abundance of pore walls, where incident EMWs undergo reflection and scattering, thereby extending their propagation path [45,46]. (III) Conductive loss: High-frequency EMWs induce internal electron migration within c-MWCNT, and electron transitions at overlapping junctions [47,48]. (IV) Dipole polarization: The oxygen-containing functional groups and intrinsic defects on the surface of c-MWCNT are capable of forming dipole pairs upon exposure to high-frequency EMWs. The rotational dynamics of these dipole pairs exhibit a lag relative to the oscillatory variation of high-frequency EMWs, thereby achieving the dissipation of EMW energy [49,50]. (V) Interfacial polarization: The hydrogen bonding interactions between c-MWCNT and ANF result in the formation of numerous heterogeneous interfaces, where the accumulation of space charge generates a capacitor-like structure that effectively dissipates electromagnetic energy [51–53]. These processes facilitate the conversion of EMW energy into thermal energy.

3.5. Multifunctionality

WGAM demonstrates exceptional thermal insulation performance owing to its ultrahigh porosity. At ambient temperature, the thermal conductivity of the aerogels was characterized using the Hot Disk technique. Initially, the thermal conductivities of WC2A1-10 mm, WC3A1-10 mm, WC4A1-10 mm, and WC5A1-10 mm were determined to be 42.2, 49.1, 58.3, and 67.4 mW m^{-1} K^{-1}, respectively (Fig. 6a). It is evident that with an increasing proportion of c-MWCNT, the 3D thermal conduction pathways constructed by c-MWCNT become more complete, leading to a gradual increment in the thermal conductivity of the composite aerogels.

Furthermore, to investigate the influence of pore structure on thermal transport properties, the thermal conductivities of RC4A1, BC4A1, and WC4A1-10 mm were measured under identical c-MWCNT content, yielding values of 50.4, 62.3, and 58.3 mW m^{-1} K^{-1}, respectively (Fig. 6b). Notably, RC4A1 exhibits the lowest thermal conductivity, whereas BC4A1 demonstrates the highest thermal conductivity. To further gain insight into the heat transfer process, COMSOL Multiphysics simulations were performed to investigate the heat transfer behaviors of three pore structure models under identical heat source conditions and heat transfer durations (relevant simulation parameters are provided in the Supplementary Material). Consistent with the experimental results, the simulation data reveal that RPA presents the slowest heat transfer rate, followed by WGAM, while BPA achieves the fastest (Fig. 6d). Moreover, temperature contour analysis at the same height section shows that RPA and BPA display relatively uniform temperature distributions, whereas WGAM exhibits a non-uniform temperature profile (Fig. S17). This phenomenon is closely attributed to the unique waxberry-like gradient pore structure of WGAM, which modulates the heat conduction paths and induces temperature variations. To elucidate the fundamental reasons underlying the aforementioned experimental and simulation results, Fig. 6e illustrates the specific thermal conduction mechanisms of aerogels with distinct pore structures, which are elaborated as follows: (I) Thermal conduction through the pore wall skeletons: In RPA, the pore wall skeletons form disordered and tortuous connections (Fig. S10a and S10b), resulting in the longest heat transfer path. Within BPA, the pore wall skeletons are continuous along the direction parallel to the orientation (Fig. S10c and S10d), thereby minimizing heat transfer distances. For WGAM, the pore wall skeletons feature radially oriented pores, and the inclined pore walls yield heat transfer paths that are longer than those in BPA yet shorter than those in RPA. (II) Thermal conduction through the gas convection: In RPA, the irregular distribution of pore walls imposes substantial resistance to gas convection, thereby impairing the thermal conduction efficiency.

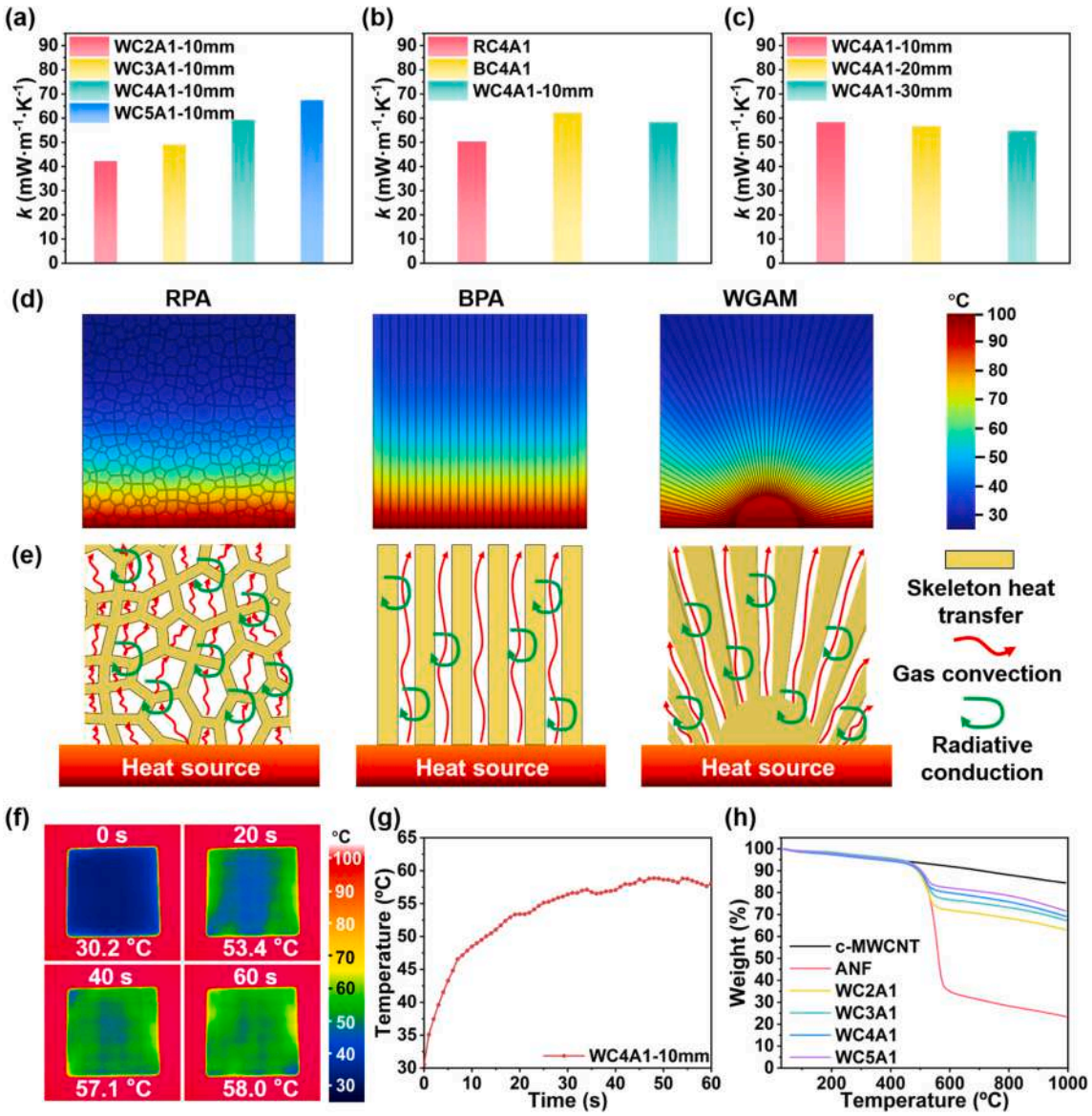

Fig. 6. Thermal properties of aerogels. Comparison of thermal conductivity of aerogels with (a) different c-MWCNT contents, (b) different pore structures, and (c) different repeating unit sizes. (d) Heat transfer simulation and (e) thermal conduction mechanisms for aerogels with different pore structures. (f, g) Infrared thermographic images and temperature-time curve of WC4A1-10 mm aerogel with a thickness of 5 mm on a 100 °C hot stage. (h) TGA curves.

Conversely, in oriented pore configurations (BPA and WGAM), gas can undergo high-velocity convection in the oriented through-pores with relatively small resistance, leading to enhanced gas-mediated thermal conduction. (III) Thermal radiative conduction: Within RPA, the disordered pore walls cause extensive radiation scattering, reducing radiative penetration and consequently diminishing thermal radiative conduction. In oriented pore structures (BPA and WGAM), the ordered arrangement of pore walls facilitates radiation propagation along the pore axis, with weakened scattering effects resulting in heightened thermal radiative conduction. Overall, the RPA exhibits a lower thermal conductivity compared to both BPA and WGAM, which can be ascribed to the longer thermal conduction pathways, stronger impediment to gas convection, and more significant scattering of thermal energy in RPA.

Likewise, the effect of repeating unit size on thermal conductivity was examined. As depicted in Fig. 6c, the thermal conductivities determined for WC4A1-10 mm, WC4A1-20 mm, and WC4A1-30 mm are 58.3, 56.7, and 54.8 mW m^{-1} K^{-1}, respectively. It is apparent that the thermal conductivity of WGAM decreases with increasing repeating unit size. This behavior can be attributed to the fact that the enlargement of the repeating unit leads to a greater inclination angle of the radial pores within WGAM, thereby resulting in an extended heat transfer path along the pore wall skeleton.

To validate the superior thermal insulation performance of WGAM, a 5-mm-thick WC4A1-10 mm was placed on a hot stage maintained at 100 °C, and an infrared thermal imager was employed to record the temperature variation on the aerogel surface (Fig. 6f and Video S2). It was observed that the surface temperature of WC4A1-10 mm increased rapidly in the initial stage, followed by the heating rate gradually decreasing, and eventually stabilized at approximately 58 °C (Fig. 6g). The surface temperature of WC4A1-10 mm after reaching thermal equilibrium was significantly lower than that of the hot stage, thereby verifying its superior thermal insulation performance.

Supplementary data related to this article can be found online at https://doi.org/10.1016/j.compositesb.2026.113399

During the supersonic flight of an aircraft at Mach 3, high temperatures ranging from 200 to 400 °C are generated at the nose due to air compression effects. To preclude the failure of aerogels under such elevated temperature conditions, the matrix material must possess

exceptional thermal stability. The thermal degradation temperatures (defined as the temperature corresponding to a 10 % weight loss) of the matrix materials and composite aerogels were evaluated via thermogravimetric analysis (TGA). The test was conducted under a nitrogen atmosphere with a temperature range spanning from ambient temperature to 1000 °C and a heating rate of 10 °C·min^{-1}. As illustrated in Fig. 6h, the thermal degradation temperatures of c-MWCNT and ANF are approximately 705 °C and 495 °C, respectively, demonstrating excellent thermal stability. The thermal degradation temperatures of c-MWCNT/ANF composite aerogels with varying filler proportions are distributed in the range of 490 °C–503 °C, which are close to that of ANF. This level of thermal stability is adequate to resist the high temperatures generated on the aircraft fuselage surface during supersonic flight at Mach 3.

For a more intuitive observation, a piece of cotton and WC4A1-10 mm were separately positioned above an asbestos mesh heated by an alcohol lamp (Fig. 7a and Video S3). It was noted that the cotton underwent rapid carbonization and shrinkage, accompanied by the emission of substantial smoke. In contrast, WC4A1-10 mm maintains structural integrity without generating copious smoke, demonstrating its excellent heat resistance. The outstanding thermal-insulating and heat-resistant properties of the WC4A1-10 mm make it capable of meeting the application requirements in extremely harsh environments.

Supplementary data related to this article can be found online at https://doi.org/10.1016/j.compositesb.2026.113399

Fig. 7b and Video S4 provide a visual illustration of the electromagnetic shielding and absorption capabilities of WC4A1-10 mm. In the experiment, a Tesla coil excites a high-frequency alternating electromagnetic field in space, which induces an electric current within the LED bulb via electromagnetic induction, successfully lighting up the LED bulb. However, when the WC4A1-10 mm is placed between the Tesla coil and the LED bulb, the LED bulb is immediately extinguished. This phenomenon confirms that the WC4A1-10 mm can block the EMWs generated by the Tesla coil from reaching the LED bulb, thereby exhibiting its functionality in shielding and absorbing EMWs.

Supplementary data related to this article can be found online at https://doi.org/10.1016/j.compositesb.2026.113399

Lightweight and high mechanical strength are of extraordinary significance and value for the engineering applications of EMWA materials. WGAM, which concurrently exhibits exceptional low density and high compressive strength, holds substantial promise for application in aircraft to reduce weight and extend range. As illustrated in Fig. 7c, the ultra-low density WC4A1-10 mm (63.1 mg cm^{-3}) can be directly placed on a fresh flower. Moreover, a mere 1.6 g of WC4A1-10 mm is capable of supporting a 1000 g weight. The mechanical strength of the aerogel was accurately measured via 30 % strain compression tests using an electronic universal testing machine. As depicted in Fig. 7d, with the increase in c-MWCNT content, the framework of WGAM becomes more robust, leading to an increase in compressive strength from 38.7 kPa to 135.3 kPa. Fig. 7e compares the compressive strengths of aerogels with different pore structures, namely RC4A1, BC4A1, and WC4A1-10 mm. The BC4A1, by virtue of the highly parallel orientation of pore structure, exhibits the highest compressive strength of 98.7 kPa. In contrast, the RC4A1, with disorderly pores, has the lowest compressive strength of only 62.6 kPa. The WC4A1, featuring radially distributed pores, has a compressive strength of 81.0 kPa, which is intermediate between those of BC4A1 and RC4A1. These results collectively indicate that the load-

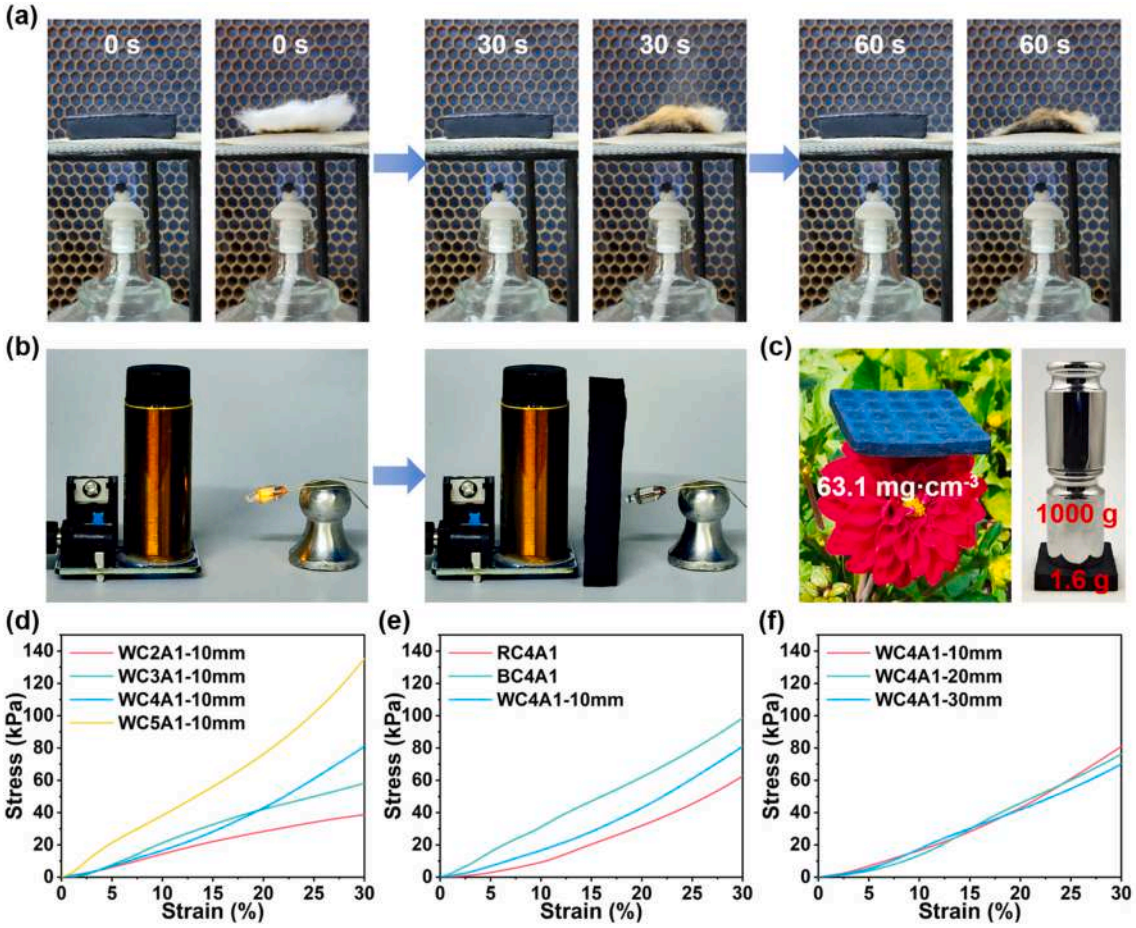

Fig. 7. Demonstration of thermal stability, EMWA, and mechanical properties of aerogels. (a) Comparison of thermal stability between cotton and WGAM. (b) Experimental demonstration of EMWA. (c) Performance demonstration of low density and high strength of WGAM. Comparison of compressive strength of aerogels: (d) different c-MWCNT contents; (e) different pore structures; (f) different repeating unit sizes.

bearing capacity of the aerogels is positively correlated with the orientation degree of their pores. Fig. 7f presents the mechanical strength characteristics of WC4A1-10 mm, WC4A1-20 mm, and WC4A1-30 mm with varying repeating unit dimensions. It is evident that as the repeating unit dimension increases, the compressive strength of the aerogels decreases from 81.0 kPa to 70.2 kPa. This is likely because the pore inclination angle of WC4A1-10 mm is relatively small, and it contains more repeating units per unit area, thus reducing the average force borne by each unit and enhancing the overall load-bearing capacity.

4. Conclusion

In summary, by configuring the cooling sources in a dot-matrix arrangement, we successfully fabricated WGAM via the innovative ice templating method. Through the integration of experimental measurements and finite element simulations, a systematic comparative analysis was performed to investigate the influences of pore structures and repeating unit sizes on the EMWA, thermal conductivity, and mechanical properties of the aerogels, thereby validating the structure-dependent behavior of the aerogels. Notably, leveraging the gradient variation between the peripheral pore size and the central core structure, WGAM exhibits an ultra-wide EAB of 12.3 GHz in the 2–18 GHz frequency band. Meanwhile, attributed to the radial distribution of pore sizes, WGAM maintains favorable EMWA performance even when the incident angle of EMWs increases from 5° to 30°. The waxberry-like pore structure of WGAM effectively mitigates the contradiction between impedance matching at the atmosphere-aerogel interface and electromagnetic loss within the aerogel matrix. Endowed with excellent thermal stability, thermal insulation, and flame retardancy, WGAM holds potential application prospects in the field of electromagnetic protection under complex environments.

CRediT authorship contribution statement

Anping Wang: Writing – review & editing, Writing – original draft, Visualization, Methodology, Investigation, Formal analysis, Data curation, Conceptualization. **Zhichun Zhang:** Writing – review & editing, Validation, Resources, Project administration, Methodology. **Yanju Liu:** Writing – review & editing, Supervision, Resources, Project administration, Funding acquisition. **Jinsong Leng:** Writing – review & editing, Supervision, Resources, Project administration, Funding acquisition.

Declaration of competing interest

The authors declare that they have no known competing financial interests or personal relationships that could have appeared to influence the work reported in this paper.

Acknowledgement

This work was financially supported by the National Key R&D Program of China (2022YFB3805700).

Appendix A. Supplementary data

Supplementary data to this article can be found online at https://doi.org/10.1016/j.compositesb.2026.113399.

Data availability

Data will be made available on request.

References

[1] Tian H, Lin J, Liu J, Li L, Li B, Zheng S, Liu W, Liu C, Zeng Z, Wu N. Ultralight SiO_2 nanofiber-reinforced graphene aerogels for multifunctional electromagnetic wave absorber. ACS Appl Mater Interfaces 2024;16(45):61484–94. https://doi.org/10.1021/acsami.4c16592.

[2] Qu H, Zheng P, Wang T, Yu X, Pan J, Fan X, Zhang T, Sun X, He J. MOF-derived multi-interface carbon-based composites with enhanced polarization loss and efficient microwave absorption. Int J Soc Netw Min 2022;13(3):465–80. https://doi.org/10.1080/19475411.2022.2095456.

[3] Wang J, Yang J, Yang J. Regulation mechanism for the formation and microwave absorbing performance of CNT/CoFe-MOF derived hierarchical composite. Int J Soc Netw Min 2022;13(2):273–92. https://doi.org/10.1080/19475411.2022.2070681.

[4] Zhao X, Li L, Li Y, Zeng J. Biobased thermoset sandwiched composites enabled by dynamic covalent chemistry for electrical insulation, EMI shielding, and thermal management. SusMat 2025;5(3):e70012. https://doi.org/10.1002/sus2.70012.

[5] Li D, Ma Q, Lin C, Liang C, Huang L, Qi Y, Li J, Zhao P, Hou Z, Zhang D, Wang G. Ultrahigh permittivity of surface-state-dominated Bi_2Te_3 nanosheets for low-frequency microwave absorption. Research 2025;8:886. https://doi.org/10.34133/research.0886.

[6] Zhang H, Meng F, Gao Y, Jin Z, Li Z, Song Z, Wang Z, Hou Y, Wang L, Zhang Q. Hierarchical ZrB_2@SiC_{nw} nanocomposite aerogel via 0D/1D/3D dimensionality expansion strategy: towards full X-band microwave absorption at high temperature. Compos B Eng 2025;306:112806. https://doi.org/10.1016/j.compositesb.2025.112806.

[7] Zhou J, Sun Y, Wu N, Han M, Liu J, Liu W, Zeng Z, Liu J. Recent advances in MXene-based aerogels for electromagnetic wave absorption. Small 2024;20(49):2405968. https://doi.org/10.1002/smll.202405968.

[8] Zhan B, Qu Y, Qi X, Ding J, Shao J, Gong X, Yang J, Chen Y, Peng Q, Zhong W, Lv H. Mixed-dimensional assembly strategy to construct reduced graphene oxide/carbon foams heterostructures for microwave absorption, anti-corrosion and thermal insulation. Nano-Micro Lett 2024;16(1):221. https://doi.org/10.1007/s40820-024-01447-9.

[9] Sun H, Yang B, Ji D, Ma C, Pang R, Yuan B, Liu J, Zhang H, Zhang M. Bioinspired aerogels: ingenious structure, remarkable performance, and versatile applications. J Mater Chem A 2024;12(21):12358–80. https://doi.org/10.1039/D4TA00851K.

[10] Su X, Gao X, Wang J, Zhang Y, Liu Y, Liu Y. Multifunctional broadband electromagnetic wave absorption through structural engineering of hierarchical aerogel-honeycomb metacomposites. Carbon 2025;243:120517. https://doi.org/10.1016/j.carbon.2025.120517.

[11] Wang J, Zhang Y, Gao X, Su X, Huang S, Liu Y. Bioinspired vascular-bundle electromagnetic management composites for low-frequency wave transmission and high-frequency wave absorption. Compos Sci Technol 2025;270:111299. https://doi.org/10.1016/j.compscitech.2025.111299.

[12] Luo J, Wang Y, Qu Z, Wang W, Yu D. Anisotropic, multifunctional and lightweight CNTs@$CoFe_2O_4$/polyimide aerogels for high efficient electromagnetic wave absorption and thermal insulation. Chem Eng J 2022;442:136388. https://doi.org/10.1016/j.cej.2022.136388.

[13] Wang A, Zhang Z, Liu Y, Li Z, Leng J. Lightweight carbon nanotube/aramid nanofiber aerogel with superior electromagnetic wave absorption, thermal insulation, and flame resistance. Carbon 2024;225:119105. https://doi.org/10.1016/j.carbon.2024.119105.

[14] Xu H, Zhan H, Xu Z, Jing C, Chen Q, Zhu M, Kong L, Fan X, Qing Y, Wen S, Wang C, Luo F. Sandwich-like CNTs/Carbon@Si_3N_4 porous foam for temperature-insensitive electromagnetic wave absorption. Adv Funct Mater 2025;35(23):2421242. https://doi.org/10.1002/adfm.202421242.

[15] Shan B, Wang Y, Ji X, Huang Y. Enhancing low-frequency microwave absorption through structural polarization modulation of MXenes. Nano-Micro Lett 2024;16(1):212. https://doi.org/10.1007/s40820-024-01437-x.

[16] Liang L, Li Q, Yan X, Feng Y, Wang Y, Zhang H, Zhou X, Liu C, Shen C, Xie X. Multifunctional magnetic $Ti_3C_2T_x$ MXene/graphene aerogel with superior electromagnetic wave absorption performance. ACS Nano 2021;15(4):6622–32. https://doi.org/10.1021/acsnano.0c09982.

[17] Lee J, Lim H, Park J, Lee J, Noh D, Jiong S, Lim DD, Choi W. Data-driven design of lightweight, interface-free metamaterial composites tailored for enhanced broadband electromagnetic absorption with robust mechanical properties. Compos B Eng 2025;306:112838. https://doi.org/10.1016/j.compositesb.2025.112838.

[18] Yang N, Gao H, Ju S, Zhang Z, Zhao Y, Guo X, Xing S, Liu J, Zhang J, Duan K, He Y. Achieving broadband electromagnetic absorption in laminated composites through progressive Bayesian optimization. Compos B Eng 2025;307:112882. https://doi.org/10.1016/j.compositesb.2025.112882.

[19] Hang T, Zhou L, Li Z, Zheng Y, Yao Y, Cao Y, Xu C, Jiang S, Chen Y, Zheng J. Constructing gradient reflection and scattering porous framework in composite aerogels for enhanced microwave absorption. Carbohydr Polym 2024;329:121777. https://doi.org/10.1016/j.carbpol.2024.121777.

[20] Zheng L, Cui K, Li W, Wang T, Wang X, Gong R. Nonlinear profile engineering of 3D-printed gradient impedance structures for broadband and strong microwave absorption. Compos B Eng 2025;305:112751. https://doi.org/10.1016/j.compositesb.2025.112751.

[21] Liang J, Zhu S, Chen D, Li Y, Zhou D, Meng N, Liao Y, Sun H, Kong J. Dual built-in electric field engineering in heterostructure nickel-cobalt bimetallic composites for boosted electromagnetic energy dissipation. Adv Powder Mater 2025;4(6):100344. https://doi.org/10.1016/j.apmate.2025.100344.

[22] Yu C, Lin D, Guo J, Zhuang K, Yao Y, Zhang X, Jiang X. Ultralight three-layer gradient-structured MXene/reduced graphene oxide composite aerogels with broadband microwave absorption and dynamic infrared camouflage. Small 2024;20(36):2401755. https://doi.org/10.1002/smll.202401755.

[23] Sun X, Li Y, Huang Y, Cheng Y, Wang S, Yin W. Achieving super broadband electromagnetic absorption by optimizing impedance match of rGO sponge

metamaterials. Adv Funct Mater 2022;32(5):2107508. https://doi.org/10.1002/adfm.202107508.
[24] Zhang Y, Pan L, Zhang P, Sun Z. Gradient multilayer design of $Ti_3C_2T_x$ MXene nanocomposite for strong and broadband microwave absorption. Small Sci 2022;2(7):2200018. https://doi.org/10.1002/smsc.202200018.
[25] Cao W, Yang L, Qi X, Hou Y, Zhu J, Yang M. Carbon nanotube wires sheathed by aramid nanofibers. Adv Funct Mater 2017;27(34):1701061. https://doi.org/10.1002/adfm.201701061.
[26] Wang M, Hu S, Bae S, Cecen V, Emre AE, Zhong Z, Liu L, Heltzel C, Huang Y, Kotov NA. Aramid nanofiber aerogels: versatile high complexity components for multifunctional composites. Adv Mater 2025;37(38):2502508. https://doi.org/10.1002/adma.202502508.
[27] Ding Y, Cheng Q, Lyu J, Liu Z, Yuan R, Ma F, Zhang X. Visible microfluidic deprotonation for aramid nanofibers as building blocks of cascade-microfluidic-processed colloidal aerogels. Adv Mater 2024;36(25):2400101. https://doi.org/10.1002/adma.202400101.
[28] Chi M, Zhang S, Liu T, Liu Y, Luo B, Wang J, Cai C, Meng X, Wang S, Duan Q, Nie S. Tunable anisotropic structural aramid triboelectric aerogels enabled by magnetic manipulation. Adv Funct Mater 2024;34(10):2310280. https://doi.org/10.1002/adfm.202310280.
[29] Wang A, Zhang X, Chen F, Fu Q. Aramid nanofiber framework supporting graphene nanoplate via wet-spinning for a high-performance filament. Carbon 2021;179:655–65. https://doi.org/10.1016/j.carbon.2021.04.056.
[30] Huang J, Li J, Xu X, Hua L, Lu Z. In situ loading of polypyrrole onto aramid nanofiber and carbon nanotube aerogel fibers as physiology and motion sensors. ACS Nano 2022;16(5):8161–71. https://doi.org/10.1021/acsnano.2c01540.
[31] Yang F, Yao J, Jin L, Huyan W, Zhou J, Yao Z, Liu P, Tao X. Multifunctional $Ti_3C_2T_X$ MXene/aramid nanofiber/polyimide aerogels with efficient thermal insulation and tunable electromagnetic wave absorption performance under thermal environment. Compos B Eng 2022;243:110161. https://doi.org/10.1016/j.compositesb.2022.110161.
[32] Zou Y, Chen Z, Guo X, Peng Z, Yu C, Zhong W. Mechanically robust and elastic graphene/aramid nanofiber/polyaniline nanotube aerogels for pressure sensors. ACS Appl Mater Interfaces 2022;14(15):17858–68. https://doi.org/10.1021/acsami.2c02538.
[33] Ma W, Liu X, Yang T, Wang J, Qiu Z, Cai Z, Bai P, Ji X, Huang Y. Strong magnetic–dielectric synergistic gradient metamaterials for boosting superior multispectral ultra-broadband absorption with low-frequency compatibility. Adv Funct Mater 2025;35(18):2314046. https://doi.org/10.1002/adfm.202314046.
[34] Shu R, Kang S, Yun K, Tian K. Fabrication of sword-shaped α-Fe_2O_3 decorated nitrogen-doped graphene composite aerogel for broadband and high-efficiency electromagnetic wave absorption. J Alloys Compd 2025;1038:182956. https://doi.org/10.1016/j.jallcom.2025.182956.
[35] Liu X, Tian K, Zhang C, Wang Q, Shu R. Controllable synthesis of pine leaf-like CoO/3D carbon foam composites as efficient microwave absorbers. Mater Res Bull 2024;176:112807. https://doi.org/10.1016/j.materresbull.2024.112807.
[36] Jiang B, Shang J, Li N, Wang Y, Hu Z, Yu J. Aramid honeycomb composites filled with rGO/BC aerogel for broadband microwave absorption and multifunctional applications. Compos Commun 2025;58:102512. https://doi.org/10.1016/j.coco.2025.102512.
[37] Ma H, Fashandi M, Rejeb ZB, Ming X, Liu Y, Gong P, Li G, Park CB. Efficient electromagnetic wave absorption and thermal infrared stealth in PVTMS@MWCNT nano-aerogel via abundant nano-sized cavities and attenuation interfaces. Nano-Micro Lett 2023;16(1):20. https://doi.org/10.1007/s40820-023-01218-y.
[38] Qi J, Zhang J, An Y, Zhang T, Wang R, Zhang W, Zhang Y, Yang Y, Xia L. Nitrogen-doped modified graphene aerogel enhancing interfacial bonding with lithium aluminium silicate ceramics for broadband microwave absorption. Carbon 2025;232:119794. https://doi.org/10.1016/j.carbon.2024.119794.
[39] Wu H, Ren X, Hu W, Tang Y, Yin H, Fan H, Yuan H, Wang C, Xin Y. Permittivity controllable CNTs/PI composite aerogels with oriented microchannels for advanced microwave absorption and thermal isolation. Carbon 2025;233:119883. https://doi.org/10.1016/j.carbon.2024.119883.
[40] Nguyen LT, Goh CJ, Bai T, Ong RH, Goh XY, Duong HM. Scalable fabrication of lightweight carbon nanotube aerogel composites for full X-band electromagnetic wave absorption. Carbon 2024;219:118811. https://doi.org/10.1016/j.carbon.2024.118811.
[41] Gao C, Gou D, Huang G, Zhang Z, Wei J, Gao F, Zhang Y, Terrones M, Chen X, Wang Y. Spiderweb-structured aerogels with high-efficiency microwave absorption and multifunctionality. Nano Energy 2025;138:110863. https://doi.org/10.1016/j.nanoen.2025.110863.
[42] Wang P, Fan D, Gai L, Hu B, Xu P, Han X, Du Y. Synthesis of graphene oxide-mediated high-porosity Ni/C aerogels through topological MOF deformation for enhanced electromagnetic absorption and thermal management. J Mater Chem A 2024;12(14):8571–82. https://doi.org/10.1039/D4TA00125G.
[43] Su X, Zhang Y, Wang J, Liu Y. Enhanced electromagnetic wave absorption and mechanical performances of graphite nanosheet/PVDF foams via ice dissolution and normal pressure drying. J Mater Chem C 2024;12(21):7775–83. https://doi.org/10.1039/D4TC00929K.
[44] Zhang X, Qiao J, Wu N, Xin G, Yue S, Ma X, Pan F, Zeng Z, Liu J. Conductive bimetal–organic frameworks with volcano-type fine-tuned dielectric properties for electromagnetic wave absorption. ACS Nano 2025;19(29):26761–9. https://doi.org/10.1021/acsnano.5c06832.
[45] Su X, Wang J, Liu T, Zhang Y, Liu Y, Zhang B, Liu Y, Wu H, Xu H-X. Controllable atomic migration in microstructures and defects for electromagnetic wave absorption enhancement. Adv Funct Mater 2024;34(39):2403397. https://doi.org/10.1002/adfm.202403397.
[46] Wu N, Yang Y, Wang C, Wu Q, Pan F, Zhang R, Liu J, Zeng Z. Ultrathin cellulose nanofiber assisted ambient-pressure-dried, ultralight, mechanically robust, multifunctional MXene aerogels. Adv Mater 2023;35(1):2207969. https://doi.org/10.1002/adma.202207969.
[47] Zhang X, Tian X, Wu N, Zhao S, Qin Y, Pan F, Yue S, Ma X, Qiao J, Xu W, Liu W, Liu J, Zhao M, Ostrikov K, Zeng Z. Metal-organic frameworks with fine-tuned interlayer spacing for microwave absorption. Sci Adv 2024;10(11). https://doi.org/10.1126/sciadv.adl6498. eadl6498.
[48] Li Y, Wang Z, Wu N, Jiao S, Che W, Han M, Lin J, Zhang K, Pan F, Liu J, Zeng Z. Enhanced electron transport in fractal conductive MOF aerogels boosting microwave absorption. Adv Funct Mater 2025:e20692. https://doi.org/10.1002/adfm.202520692.
[49] Zhang Y, Wang J, Wu Q, Shan T, Bai S, Lan D, Zhang B, Liu Y, Su X. Enhanced electromagnetic wave absorption of bacterial cellulose/reduced graphene oxide aerogel by eco-friendly in-situ construction. J Colloid Interface Sci 2025;678:648–55. https://doi.org/10.1016/j.jcis.2024.08.211.
[50] Wei M, Wu N, Li B, Liu J, Pan F, Liu J, Zeng Z. From MXene to multimodal-responsive smart, durable electromagnetic interference shielding textiles. Adv Funct Mater 2025;35(28):2424312. https://doi.org/10.1002/adfm.202424312.
[51] Ding X, Zhao X, Zhang J, Wang B, Tian K, Shu R. Fabrication of chitosan/MIL-88A derived nitrogen-doped carbon/ferroferric oxide/carbon composite aerogels for electromagnetic wave absorption and thermal insulation. Carbon 2026;246:120957. https://doi.org/10.1016/j.carbon.2025.120957.
[52] Yun K, Shu R, Yi X, Tian K. Nitrogen-doped reduced graphene oxide/copper ferrite@polypyrrole composite aerogels for broadband electromagnetic wave absorption. Chem Eng J 2025;518:164748. https://doi.org/10.1016/j.cej.2025.164748.
[53] Lin J, Liu J, Zhang K, Deng Y, Che W, Pang X, Zhang Q, Cai W, Zeng Z, Wu N. Ambient-pressure-dried aerogel amplifies interfacial polarization toward high-efficiency microwave absorption. Adv Funct Mater 2025:e20336. https://doi.org/10.1002/adfm.202520336.